

Quantum Circuit Fidelity Improvement with Long Short-Term Memory Networks

Yikai Mao,^{1,*} Shaswot Shresthamali,¹ and Masaaki Kondo^{1,2}

¹Graduate School of Science and Technology, Keio University, Yokohama, Kanagawa 223-8522, Japan

²RIKEN Center for Computational Science, Kobe, Hyogo 650-0047, Japan

(Dated: May 5, 2023)

Quantum computing has entered the Noisy Intermediate-Scale Quantum (NISQ) era. Although NISQ computers show great promise in accelerating many tasks that are not practically possible using classical computation, useful quantum computing is still a long way off. One important reason is due to the fragile nature of quantum hardware. As the building blocks of a quantum circuit (QC), quantum gates and qubits are susceptible to external interference, and therefore even a simple QC can produce extremely noisy output. Since it is hard to distinguish whether the output represents meaningful computation or just random noise, it raises the question of how much we can rely on the output of a QC, i.e., the fidelity of the QC. In this paper, we propose a simple yet intuitive metric to measure the fidelity of a QC. By using this metric, we can observe the evolution of fidelity with time as the QC interacts with its external environment. Consequently, we can frame fidelity prediction as a Time Series Forecasting problem and use Long Short-Term Memory (LSTM) neural networks to better estimate the fidelity of a QC. This gives the user better opportunities to optimize the mapping of qubits into the quantum hardware for larger gains. We introduce the LSTM architecture and present a complete workflow to build the training circuit dataset. The trained LSTM system, Q-fid, can predict the output fidelity of a QC running on a specific quantum processor, without the need for any separate input of hardware calibration data or gate error rates. Evaluated on the QASMBench NISQ benchmark suite, Q-fid's prediction achieves an average RMSE of 0.0515, up to $24.7\times$ more accurate than the default Qiskit transpile tool `mapomatic`. When used to find the high-fidelity circuit layouts from the available circuit transpilation, Q-fid predicts the fidelity for the top 10% layouts with an average RMSE of 0.0252, up to $32.8\times$ more accurate than `mapomatic`.

I. INTRODUCTION

To outperform classical computers, quantum computers make use of the principles and phenomena of quantum mechanics. Traditionally, computers manipulate their classical bits in the binary basis, or 0/1 basis. When operating a quantum computer with qubits, in addition to representing the classical 0/1 with its computational basis $|0\rangle/|1\rangle$, the qubits also have the ability to switch to any desired basis, elevating the calculation to a higher dimension. Moreover, by entangling multiple qubits, the computation can be performed simultaneously in an exponentially larger space. This gives quantum computers the potential to achieve superpolynomial or even exponential speedups for traditionally hard computing problems, for example, Simon's problem [1].

Ever since Google fabricated the Sycamore processor back in 2018 and later claimed to have achieved quantum supremacy in 2019 [2], the field of quantum computing hardware has grown substantially. However, the current state of quantum computing is still far from perfect. This is because quantum computers are easily affected by external noise. Present day quantum computers have a limited amount of qubits with limited inter-connectivity and very short coherence lifetimes (in order of milliseconds) [3, 4]. Furthermore, the gate operations and read-out are very susceptible to noise. To overcome the noise limitations of today's machines, Noisy Intermediate-Scale

Quantum (NISQ) [5] offers a viable solution. NISQ computing uses error-mitigation techniques to compensate for fragile qubits [6–8]. For example, performing repeated measurements to find high-probability outputs, or using multiple noisy physical qubits to represent one robust logical qubit [9, 10].

To implement a quantum circuit on a real NISQ processor, the circuit must be mapped onto the available physical qubits in accordance with the connectivity configurations that are possible in the hardware. [11, 12], a process commonly known as transpilation. However, there are several challenges during this process. First, the qubits in one processor are not identical. Each of them has unique physical properties, typically categorized as $T1/T2$ (Thermal relaxation time) constants. These physical properties define the noise characteristics of the qubit, and they can change depending on the time of operation. *So it is possible for the same abstract quantum circuit to have drastically different noise characteristics when mapped to different qubit configurations.* Second, due to the limited qubit connectivity, some quantum circuits need to be modified from the original design before implementing on real hardware. For example, we may need to add SWAP gates to bring two physically distant qubits together for a two-qubit gate operation and then return them back to their original positions. *Consequently, the accuracy of a quantum circuit can get compromised even if it is placed on high-quality qubits, due to the additional gate noise introduced by circuit transpilation.* Therefore, **to make the best use of current NISQ processors, we need a method to accurately pick a high-fidelity circuit-**

* ykmao@acsl.ics.keio.ac.jp

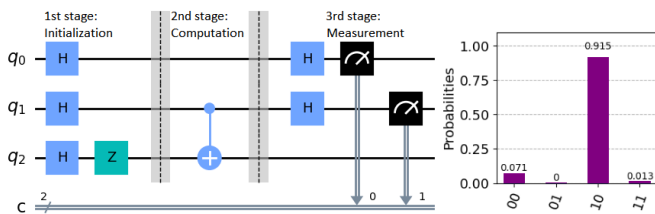


FIG. 1. Sample Circuit implementing the Bernstein-Vazirani Algorithm, the expected output should be $q_1q_0 = |10\rangle$. q_2 is not measured so the output is a 2-bit number. Output distribution after running the circuit for 1,024 times on real hardware (*ibm_nairobi*) is plotted on the right, the correct state $|10\rangle$ has been measured 937 times, but the wrong measurements $|00\rangle$ and $|11\rangle$ also appears in the distribution due to noise.

to-qubit mapping from all the transpiled options.

This way we can efficiently retrieve high-quality measurements, without wasting quantum computing resources on testing noisy, error-prone transpilations.

The study of quantum circuit performance on real devices is still a very active area of research, and quantum hardware providers are already offering tools to optimize circuits using simple noise models. One such tool to estimate the fidelity of a quantum circuit is *mapomatic*, integrated inside the standard Qiskit transpiler [13]. *mapomatic* estimates circuit fidelity by accumulating the individual gate error rates, obtained from the Randomized Benchmarking (RB) [14] protocol. This approach has some severe limitations. First, the RB experiments must be performed frequently to keep the gate error rates up to date. Second, the noise characteristic of a full quantum circuit is not simply the product of the individual gates, as there still exists many error structures that are unmodeled [15]. Due to these limitations, *mapomatic* cannot estimate the fidelity accurately and it only gives the relative performance comparison for a set of circuits with different physical mapping.

In this work, we present a new metric, $d-R^2$, that faithfully represents the fidelity of the quantum circuit. Based on this metric, we then develop an LSTM-based system: Q-fid, to accurately predict the fidelity of a quantum circuit. It eliminates the need for frequent calibration and Randomized Benchmarking experiments by actively learning qubit/gate operations from circuit execution data, without any separate input of system calibration parameters or error rates. Since the only input to Q-fid is the quantum circuit, it can be used on any gate-based quantum computer regardless of their implementation technology.

Traditionally, a NISQ circuit requires hundreds to thousands of shots on a real processor to statistically estimate its correct output. With Q-fid, we can choose which circuits have higher fidelity and reject low-fidelity ones. By doing so, we can obtain the solution with fewer but higher-fidelity shots and thus save precious quantum computing resources.

We trained Q-fid on two of the IBM quantum pro-

cessors: *ibm_nairobi* and *ibmq_montreal*. We used the QASMBench benchmark suite [16] with 25 NISQ algorithms from simple to complex to test Q-fid’s accuracy and compared it with *mapomatic*. We ran individual circuits with fixed layouts and no transpiler optimizations on *ibm_nairobi*. Q-fid was able to predict the circuit’s fidelity with an average RMSE of 0.0515, which is $5.70\times$ better than *mapomatic*. Among the 25 tested algorithms, Q-fid is more accurate than *mapomatic* by as much as $24.7\times$. On *ibmq_montreal*, when transpiler optimization is on, Q-fid correctly finds the top 10% of high-fidelity circuit layouts for all 25 algorithms. Within those top 10% of layouts, Q-fid’s predicted fidelity has an average RMSE of 0.0252, up to $32.8\times$ more accurate than *mapomatic*.

The contributions of this work are listed below:

- We propose a simple and intuitive method to model a quantum circuit as a **text-based time series**. This method enables feeding the quantum circuits directly into an LSTM neural network, and it can be applied to **any gate-based quantum processor**, regardless of their implementation technology.
- We present the **discrete coefficient of determination** ($d-R^2$) as a new metric to quantify the fidelity of a noisy quantum circuit. $d-R^2$ clearly defines the uniform distribution as the **worst-case** output distribution for a quantum circuit, offering an intuitive baseline comparison for NISQ algorithm fidelities.
- We show that LSTM is effective in learning the properties of a qubit and a quantum gate from the quantum circuit itself. The trained system, **Q-fid**, can predict the performance of a quantum circuit without any separate input of hardware calibration data or gate error rates.
- We provide a **framework** to use LSTM for on-the-fly quantum circuit fidelity estimation, including the **architecture** of the neural network, how to build the **dataset**, and the training **workflow**. We show that Randomized Benchmarking can be used to generate a comprehensive dataset for initial training set.
- Experiments on **real NISQ algorithms** show that because Q-fid can accurately predict the fidelity of quantum circuits, we can retrieve more **high-fidelity, usable transpilations** than *mapomatic* from a large set of transpiled circuits, thus increasing processor utilization by allowing more circuit placement options.



FIG. 2. (a) Error map of *ibm_nairobi* on Dec. 9, 2022, generated by the IBM Q platform [17]. (b) T_1/T_2 fluctuation of the 7 physical qubits inside *ibm_nairobi*. 100 data points were collected from Aug. 25 to Dec. 18, 2022. Note that data is not continuous due to scheduled/unscheduled system maintenance, for example around Nov. 1.

II. BACKGROUND

A. Quantum Circuits

Quantum computers can be broadly classified into quantum annealers and universal gate-based processors. In this work, we concern ourselves with only gate-based computers. In a gate-based quantum computer, the quantum bits (or qubits) are manipulated by a sequence of quantum gate operations as described by the quantum circuit (QC). These gates change the state of the qubit and the transformations can be expressed by unitary matrices i.e., the computation is reversible.

Typically, executing a QC involves three stages: state preparation, computation, and measurements. During state preparation, the input qubits are initialized into a specific state, and typically put into superposition. Then they enter the computation stage where the sequence of gates described by the quantum circuit manipulates the states of the qubits. Finally, the qubits of interest are measured, bringing them back from the quantum basis to the computational basis to reveal the classical information.

Figure 1 shows a sample implementation of the Bernstein-Vazirani Algorithm [18], divided into three stages: In the first stage, the qubits are initialized to $|-\ +\ +\ \rangle$ from $|000\rangle$. Once initialized, the gate operation (CNOT) is performed. Finally, in the third stage, the qubits are returned to their original basis using Hadamard gates and then measured into the classical registers c_1c_0 to store the output.

B. NISQ Processors

Most superconducting quantum processors use the NISQ processing paradigm in which multiple physical qubits are used to represent one logical qubit. Furthermore, these qubits have fixed and limited connectivity. For example, Figure 2(a) gives the connection map of the 7-qubit quantum processor *ibm_nairobi* along with three major forms of possible error: readout, single-qubit er-

ror, and CNOT error. As shown in the connection map, qubit 2 has the worst readout error rate and H gate error rate. The CNOT connections between qubits 3 to 5 and qubits 1 to 2 are also significantly noisier than others.

These error rates are usually obtained by Randomized Benchmarking and the errors are expected to vary over time. It is very difficult to model these errors completely because qubits are very sensitive to multiple sources of noise whose effects and origins are many and unknown.

Other mathematical models exist to characterize qubit qualities, and most of them involve measuring their T_1/T_2 constants. T_1 is commonly called the coherence time, which describes how long it takes for a qubit to relax from an excited state to the ground state. T_2 is the decay time, which describes how long it takes for a qubit to lose its phase information. However, as shown in Figure 2(b), the T_1/T_2 constants can also fluctuate significantly, and it is hard to predict which physical qubit is more stable than others at a given time.

C. Randomized Benchmarking

Randomized Benchmarking (RB) [14, 19] is a protocol to estimate the error rates of the set of common quantum gates, usually called the Clifford gates. For IBM Q devices, this Clifford gate group includes [X, Z, P, H, CNOT, CZ, SWAP] [20]. Based on the reversible principle of quantum gates, the RB protocol first generates a QC containing random quantum gates in the Clifford group, then it calculates a complementary gate sequence that can reverse the computation performed in the first QC. An example RB circuit is given in figure 3. By applying the two generated QCs back-to-back, the full circuit is equivalent to an identity operator so ideally any qubits involved in this circuit should never change their states when measured at the end.

However, when executing an RB circuit on a NISQ processor, it is possible that the qubits cannot return to their initial state due to the noisy nature of the hardware. Therefore, by repeatedly running RB circuits and measuring the qubit outcomes, we can estimate the av-

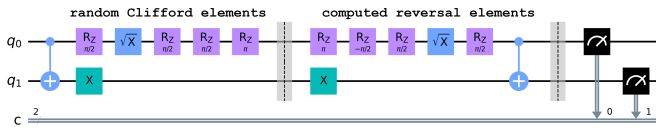


FIG. 3. Example of a Randomized Benchmarking circuit. The first part is the randomly generated Clifford gates, followed by the calculated reversal gates. The final measurement should be $|00\rangle$ if no errors occurred.

erage fidelity of the processor, and use that information in turn to predict the gate error rate, either for 2-qubit gates or single-qubit gates.

D. Circuit Transpilation

Due to the limited connectivity of current NISQ processors, it is not always possible to map a complex QC onto the processor directly. Take the connection map from Figure 2(a), notice the physical CNOT links exist only between neighboring qubits. So if a QC requires a CNOT gate between qubit 0 and qubit 3, additional operations must be added to the QC to compensate for the missed connection. This process of translating a hardware-agnostic QC description to implement in a given hardware platform is referred to as transpilation.

To perform a long-distance CNOT gate in a superconducting quantum computer like *ibm_nairobi*, the transpiler can insert SWAP gates to switch the position of the nonadjacent physical qubits to use the existing CNOT links. However, in addition to connectivity restrictions, real quantum processors also have limited single-qubit gate availability. For example, *ibm_nairobi* only supports four single-qubit gates: ID, RZ, SX, X. Therefore, To perform a single-qubit operation like the Hadamard gate, the transpiler will need to decompose the operation into the gates available in the processor.

Typically, some level of QC optimization is also performed by the transpiler. One common optimization technique is CNOT reduction: because the SWAP gate is realized by three consecutive CNOT gates, it usually creates redundant gates that cancel each other due to the reversible nature of quantum operations, so they can be removed from the QC without affecting the final output states.

E. Long Short-term Memory Network

Neural Networks (NN) have demonstrated state-of-the-art performance in various tasks including Computer Vision (CV) and Natural Language Processing (NLP). Among numerous NN architectures, Long Short-term Memory (LSTM) networks [21] have been a popular choice for tasks related to time series processing, for example, weather forecasting and sentiment prediction.

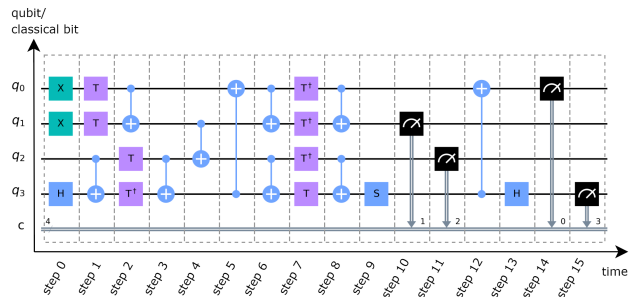


FIG. 4. Quantum circuit placed in a coordinate system with the y-axis as qubit/classical bit, and the x-axis as time. It can be viewed as the qubits being manipulated through each timestep from the left to the right on the time axis.

In this work, we leverage the ability of LSTMs to learn temporal relationships in sequential data to estimate circuit fidelity with high accuracy. It is very easy to see that quantum circuits are in essence sequential gate operations that operate on qubit(s). There is an inherent temporal sequence in the execution of qubits. Furthermore, the fidelity of the entire circuit not only depends on the individual gate/qubit characteristics but also on how they interact with each other as the circuit progresses towards completion - much like words in a sentence or notes of a musical score. Since LSTMs are trained to recognize these types of temporal relationships, we use them to estimate circuit fidelity in this work. As to our knowledge, this is the first work that uses LSTM for fidelity estimation.

As figure 4 shows, the x-axis can be used to indicate the timesteps of a QC from start to end, with each timestep modeled as a “QC layer” containing all the gates in the y-axis. The layers act on the same set of qubits and have fixed widths, so the QC can be described as a two-dimensional time series with its width equal to the number of qubits in the circuit, and its length equal to the number of layers (sometimes referred to as the depth) of the circuit.

III. PROPOSED Q-FID FRAMEWORK

A. Framework Description

Q-fid is an LSTM network that takes a QC as input and predicts the output fidelity of this QC running on real hardware. Inspired by one of the most popular LSTM applications, Sentiment Analysis [22], the workflow of Q-fid is very similar to the workflow of many common NLP tasks. In these tasks, the LSTM takes a sentence as input and gives a prediction based on different goals. For example, translate the sentence into another language, return the answer to the sentence if it is a question, or whether the expressed sentiment is positive or negative. Although every individual word has its own definition, once combined together, they become elements of a sin-

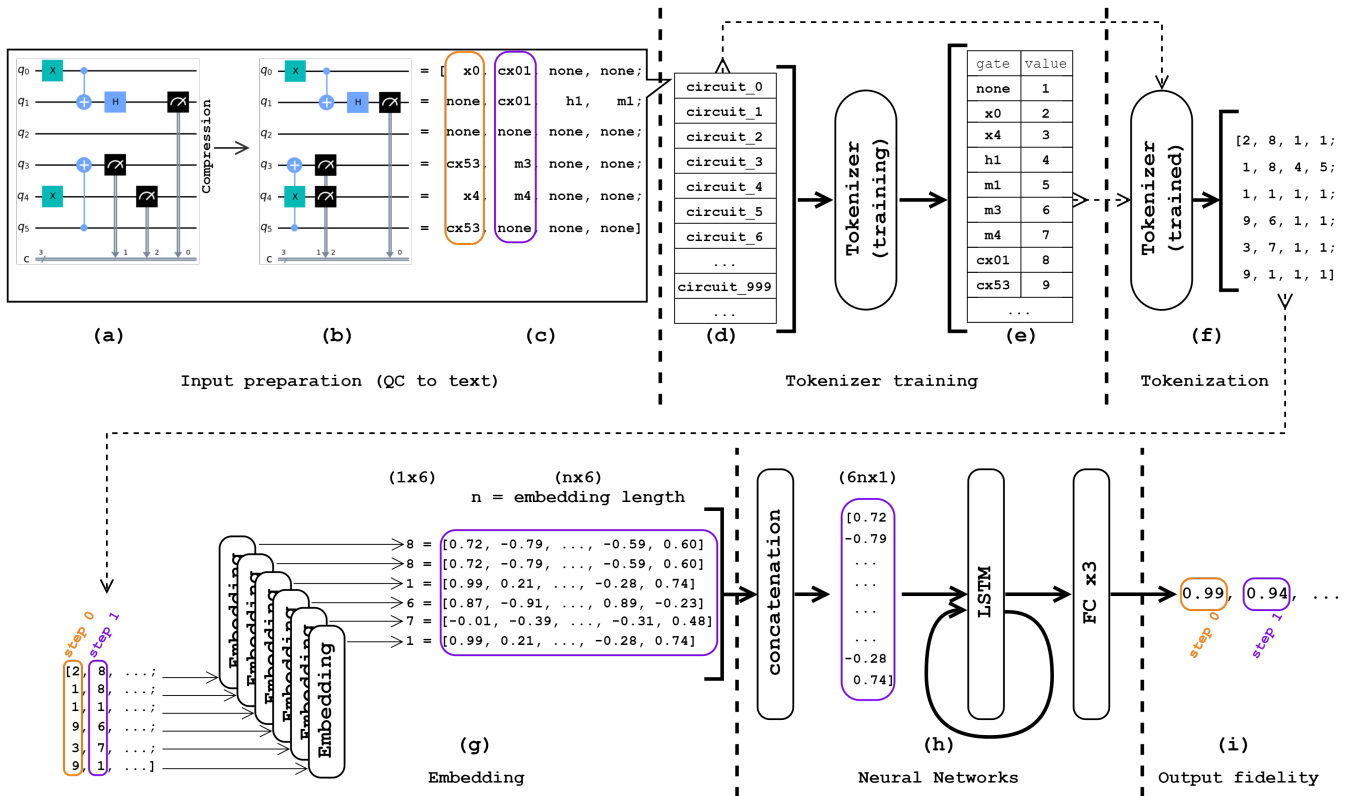


FIG. 5. Overview of Q-fid’s workflow. The first stage is input preparation (a, b, c), where the quantum circuits are compressed and mapped to their corresponding text label. The second stage is tokenizer training (d, e), the tokenizer will look through all the circuits in the dataset and assign each text label with an integer according to their appearing frequency. After the tokenizer is trained, it will use its internal dictionary to translate all of the circuits in the dataset to an integer representation, which is called tokenization (f). Q-fid’s neural network uses embedding (g) and LSTM (h) layers to encode the integer labels and then extract sequential and relationship information from the circuit, each prediction (i) is associated with one timestep in the circuit, when all the timesteps are processed by the LSTM, the output will be the final fidelity prediction for the full circuit.

gle sentence where the meaning of the sentence must be inferred from the relationship between all of the words.

This concept fits surprisingly well when applied to a QC: Although every individual quantum gate has its own operation and noise characteristics, once combined together, they become elements of a single circuit where the computation and fidelity of the qubits must be measured after all quantum gates have been executed. Similar to a sentence where different orders of the same words can express different sentiments, the same set of quantum gates can perform different computations and express different fidelity depending on their order in a circuit. Q-fid uses LSTM to catch this long-term temporal dependence and noise characteristics inside a QC.

At the core of the proposed Q-fid framework is an LSTM network with a simple and lightweight architecture. The input layers first perform general pre-processing of the input QCs, then they are passed into the LSTM layer to extract long-term and short-term noise dependencies between the gates inside the QC. Finally, the output from the LSTM layer is passed into a series of fully-connected layers to generate the final prediction of the circuit fidelity. An overview of Q-fid’s LSTM ar-

chitecture is shown in figure 5 from (g) to (i).

A distinctive feature of Q-fid is that it does not require any prior knowledge of the processor’s calibration data ($T1/T2$, frequency, etc.) to make predictions. Because the LSTM infers the hardware noise characteristics from the input QC, the user does not need to supply any other information to Q-fid. This hardware-agnostic feature gives Q-fid several advantages over the other calibration-based prediction systems. First, since the hardware descriptions are abstracted away, Q-fid can work with any gate-model quantum computer, regardless of whether the qubit is implemented with superconducting circuits or trapped ion. Second, when training Q-fid, the training label (fidelity) corresponding to the input QC is a comparison of the two output probability distributions: one produced by a noise-free simulation of the QC, the other one produced by executing the QC on the noisy hardware. Notice that the user does not need to specify any device calibration data for these two executions, which means Q-fid can be trained dynamically during regular workload and adapts to the ever-changing device characteristics, all without interruptions caused by calibration or maintenance jobs.

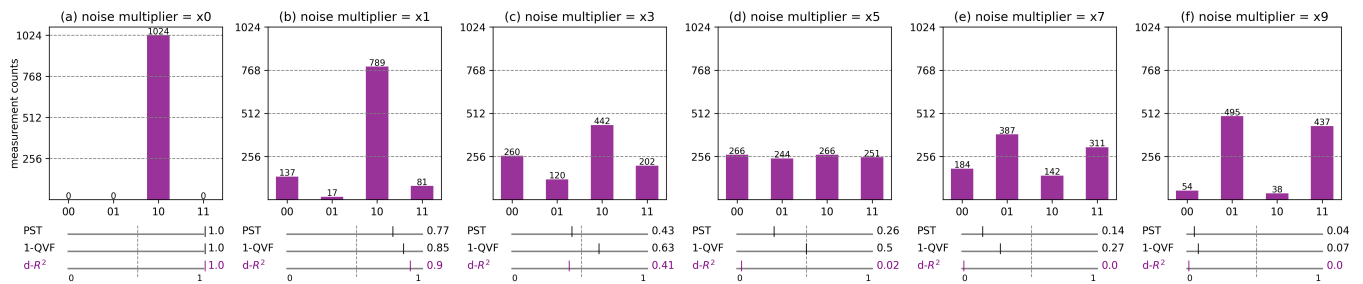


FIG. 6. Output distributions after executing the circuit in figure 1 with 1,024 shots using various noise models. The base error rates for gates, measurements, and reset are set as: $0.05n$, $0.1n$, and $0.03n$. n is the noise multiplier where $\times 0$ means noise-free and $\times 10$ is the maximum possible value. The comparison of three QC fidelity metrics is shown below the bar graph, where 1 means perfect circuit fidelity. (a) is the noise-free output, the correct output state should be $|10\rangle$. (b) to (f) are the outputs under different noise multiplier values. The output in (d) is a uniform distribution, which gives zero information on which state might be the correct state. (f) is considered as a faulty output, the circuit is not doing the intended quantum operations so the wrong states are appearing more than the correct state.

B. Discrete Coefficient of Determination ($d-R^2$)

The LSTM updates its NN parameters by comparing the differences between the true output probability distribution of the QC and the observed output distribution. We thus need a single metric that represents this difference so that we can feed it into the loss function of the LSTM network. In this paper, we propose a slightly modified version of the *coefficient of determination* (R^2) as the standard metric for evaluating noisy QC fidelity. R^2 is commonly used in regression analysis to show the quality of how well a fitted line represents the original data, and it has been proven to be more robust and reliable than the other mean error-based metrics (MSE, MAE, etc.), especially on poor quality regressions [23]. Typically, $R^2 = 0$ indicates that the fitted line does not represent the original data at all, and $R^2 = 1$ indicates a perfect fit.

Recent works [12, 24] use the Probability of Successful Trials (PST) as a metric to quantify the performance of a noisy QC, which is defined as the ratio of the *number of successful trials* to the *total number of trials*. Although PST is easy to calculate, it does not give the user enough information to analyse the circuit. For example, figure 6(e) shows a distribution where PST gives a fidelity score of 0.14. However, the user cannot distinguish whether this low fidelity is caused by $|00\rangle$ or $|10\rangle$, due to their similar measurement counts. Other metrics have been proposed to replace PST, for example, the Quantum Vulnerability Factor (QVF) [25] and the Total Variation Distance (TVD) [26]. However, they do not offer a clear definition when multiple correct states are expected, which often happens for common NISQ algorithms like QAOA [27] and VQE [28].

In another scenario where the QC outputs a uniform superposition like figure 6(d), PST and QVF will yield a fidelity score of 0.26 and 0.50, respectively. However, the uniform superposition does not give any useful information about which state should be the correct state as all the states have the same probability. More importantly,

a uniform superposition can be easily generated by applying Hadamard gates to all the qubits, which renders the computation performed in the original QC meaningless [29]. Since distributions worse than a uniform superposition indicate wrong result (e.g. figure 6(e) and (f)) and should not be used to interpret the computation, we argue that the uniform superposition should be defined as the worst case output and have a 0 score in terms of fidelity.

Our modified version of R^2 is called discrete- R^2 , or $d-R^2$. compared with the other aforementioned metrics, $d-R^2$ has two important features that make it more suitable for NISQ fidelity analysis. First, it takes all the states in the distribution into consideration. So in addition to checking how well the correct states are standing out, $d-R^2$ also penalizes wrong states when they should not appear in the output distribution, which makes it work well with algorithms that output multiple correct states. Second, the baseline comparison model of the original R^2 metric ($R^2 = 0$) is the average line of the original distribution. In $d-R^2$, this average line over the noise-free output distribution exactly represents the uniform superposition, which conveniently matches our argument: a uniform superposition should be the worst-case output from a noisy QC.

To calculate $d-R^2$, we first have to calculate two Sum of Squares (SS):

$$SS_{residual} = SSR = \sum_{i=0}^{2^n} (Y_i - y_i)^2 \quad (1)$$

$$SS_{total} = SST = \sum_{i=0}^{2^n} (Y_i - \text{mean}(Y))^2$$

Here, n is the number of measured qubit(s), Y is the distribution containing all the measurement counts from the **noise-free** output, and y is the distribution containing all the measurement counts from the **noisy** output. For example in figure 6(b), Y would be $(0, 0, 1024, 0)$ so

$mean(Y)$ is 256, and y would be (137, 17, 789, 81). Note that when calculating the subtractions, Y and y must be aligned so that the measured states match each other. Then $d-R^2$ can be obtained as:

$$d-R^2 = \begin{cases} 1 - \frac{SSR}{SST}, & \text{if } SSR < SST \\ 0, & \text{otherwise} \end{cases} \quad (2)$$

- It is possible for $d-R^2$ to be negative without the bounding condition $SSR < SST$, this indicates that the distribution fits worse to the correct distribution than a uniform superposition, possibly caused by extremely noisy qubits or hardware faults. Figure 7 shows the negative region of $d-R^2$ when the noise multiplier is larger than $\times 5$.
- A special case where $d-R^2$ is undefined happens when $SST = 0$ in equation 1. In the context of quantum computing, this indicates that the QC is **designed** to output a uniform superposition. This kind of circuit has some important applications, for example, it can be used as a Quantum Random Number Generator (QRNG) [30]. In this case, $d-R^2$ becomes undefined by design because the QC should not be evaluated based on its fidelity, but rather on uniformity or randomness.

The interpretations for different $d-R^2$ values used in this paper are given in table I.

| $d-R^2$ | Interpretation |
|---------------------|--|
| = 1 | output is perfect, same as if there was no noise. |
| > 0.7 to ≤ 1 | output is good, the circuit has high fidelity. |
| > 0.5 to ≤ 0.7 | output quality is fair, contains noticeable noise. |
| > 0.3 to ≤ 0.5 | output contains significant noise, interpret with caution. |
| > 0 to ≤ 0.3 | output is extremely noisy, do not use. |
| = 0 | output is no better than a uniform superposition. |

TABLE I. discrete- R^2 values and interpretations

C. Text-based Representation of Quantum Circuits

We represent QC in text string formats that are suitable for feeding into the LSTM networks. Q-fid uses a simple and effective protocol to label the quantum gates inside a QC: a short string describing the quantum operation followed by the qubit index describing where the operation is executed on. For example, a Hadamard gate placed on qubit 2 is simply labeled as `h2`, a CNOT gate with control on qubit 0 and target on qubit 3 will be `cx03`. This format is very similar to many existing quantum programming languages including openQASM and Qiskit, so preparing the text representation of an existing QC for Q-fid is straightforward.

Q-fid has three steps to translate the QC to an LSTM-friendly format, a process commonly referred to as tokenization:

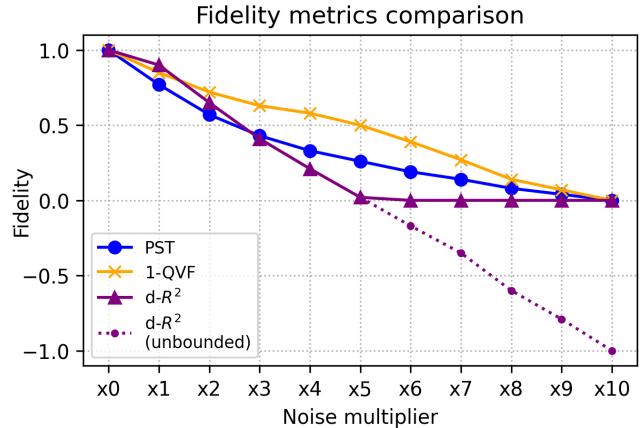


FIG. 7. Fidelity metrics comparison when different noise multiplier values are applied on the circuit in figure 1. Note that $d-R^2$ can go to the negative region if the bounding condition in equation 1 is removed.

1. A tokenizer reviews the full QC dataset and builds a dictionary that maps each text label of a quantum gate to a unique integer. The labels are ranked according to the frequency they appear in the circuit, with the most common appearing label mapped to 1. A special label in Q-fid is `none`, which means the qubit is staying idle. This label is important because the qubit can decay and become noisier even when no gates are applied. An example of this workflow is shown in figure 5 from (a) to (f).
2. For a large QC dataset, the depth of the individual QCs can vary a lot. To improve the accuracy and efficiency of LSTM training, it is better to fix the number of time steps in the dataset. Once the maximum number of time steps is set, all of the integer-based QC vectors are either truncated or padded to the same depth. Specifically, the reason for the tokenizer to start from 1 is that 0 is reserved as the padding element, so that the LSTM knows it is not a label for a quantum gate and can safely skip it. We follow the common practices in NLP [31] to use pre-padding and post-truncation.
3. After all the text labels are converted to integers, every QC in the dataset is now a dense vector. However, this is still not an efficient representation for input to Q-fid. The integers do not possess any relationship or similarity information between different gates, so it is hard for the LSTM to learn the effect of interconnected quantum gates. This problem is solved by using word embeddings, a technique of using a higher dimension fixed-length vector to replace the integer encoding [32]. The values of this embedding vector are trained at the same time with the LSTM, which helps Q-fid capture more detailed information from the QC. The embedding layers are shown in figure 5(g).

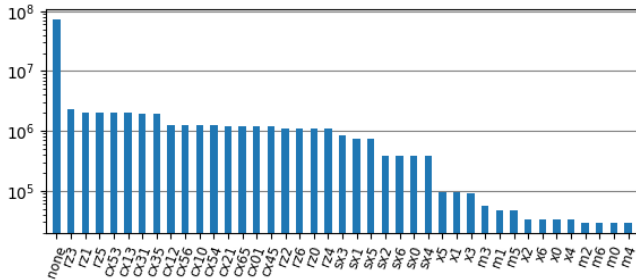


FIG. 8. The number of appearances for all the gate labels in the *ibm_nairobi* dataset. “m” stands for “measure”, so m0 means measure gate on qubit 0. The most common label is “none” with 72, 124, 510 appearances, and the least common label is “m4” with 29, 528 appearances.

D. Training Circuits and Dataset for Q-fid

Training Q-fid requires a large QC dataset that is also diversified in circuit depth and width, as the relationship between fidelity and circuit size is not necessarily linear. Although a deeper QC tends to have a lower fidelity, its output is not always unusable. Some deep but simple algorithms like the Quantum Phase Estimation (QPE) algorithm can be executed on noisy hardware and still give an output that is very likely to be the correct answer. Conversely, a shallow QC using multiple qubits with complex connections will experience a higher error rate than a QC only using one qubit with no CNOT connection.

In this work, we utilize the RB protocol to efficiently create a QC dataset to train Q-fid. Because the gates in RB circuits are randomly generated, they span over all different types of gates, depths, widths, and qubit interactions. This provides the required diversity of width and depth for the dataset. Most of the computing complexity for generating RB circuits comes from calculating the final circuit block that reverses the previous operations, and it can be calculated efficiently in polynomial time, proved by the Gottesman-Knill theorem [33].

Using RB circuits in training provides many benefits, one of the advantages is that it greatly simplifies fidelity calculation. Every RB circuit is by definition equivalent to an identity operator, so if the qubits are initialized to $|0\dots0\rangle$, we know the ideal output states must also be $|0\dots0\rangle$. This means that in order to calculate the ground-truth training labels ($d-R^2$) for an RB circuit, we only need to obtain one noisy output distribution of the circuit.

Figure 8 gives the gate statistics of one training dataset generated on the quantum processor *ibm_nairobi* using the RB protocol. We see that all the available gate operations and qubits on *ibm_nairobi* have been sufficiently covered. Thus we can be assured that the trained Q-fid model is not biased.

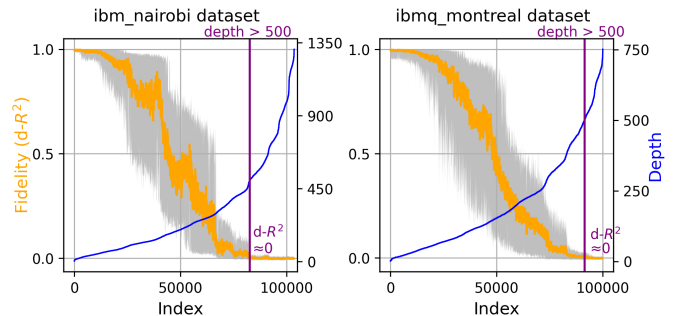


FIG. 9. Two QC datasets showing the fidelity of a QC decreases with increasing depth. The x-axis represents the indices of RB circuits ordered from the shallowest to the deepest ones, with a vertical purple line indicating the cut-off point of $depth = 500$. The fidelity has a very large variance so the raw data is plotted using a gray envelope and an orange average line.

IV. EXPERIMENTAL METHODOLOGY

A. Dataset

We created two datasets based on two real IBM Quantum processors, *ibm_nairobi* and *ibmq_montreal*. The QCs are randomly generated using the RB protocol, with the length of the RB sequence ranging from 1 to 5. We also change the number of active qubits when generating the RB circuits. For example, even though *ibm_nairobi* is a 7 qubit processor, we generated RB circuits that only require 1 qubit, 2 qubits, etc. The main reason for doing this is because placing the QC on different physical qubits on the same processor can yield different fidelity due to noise and manufacture variation. When the RB circuit only requires 1 active qubit, we can place the circuit on 7 different physical qubits on *ibm_nairobi*. This improves Q-fid’s ability to learn the properties of individual qubits.

The *ibm_nairobi* QC dataset contains 103,500 circuits, and the *ibmq_montreal* QC dataset contains 100,000 circuits. All of the circuits are transpiled and converted to a text-based representation described in section III C, then the fidelity of the circuits are calculated by obtaining the noisy output distribution using the Qiskit Aer simulator, with a noise model generated from the real hardware device. We constrain the depth of the circuits to be less than or equal to 500 because circuits deeper than 500 have near-zero fidelity, as shown in figure 9. After trimming, the *ibm_nairobi* QC dataset has 82,644 circuits, and the *ibmq_montreal* QC dataset has 91,386 circuits.

B. Model and Training

We build two Q-fid models to test the two processors, the architecture of Q-fid for *ibm_nairobi* is shown in figure 10. Each qubit has its own input layer and they all have a length of 500, equal to the maximum QC depth of the dataset. The embedding layer transforms every gate

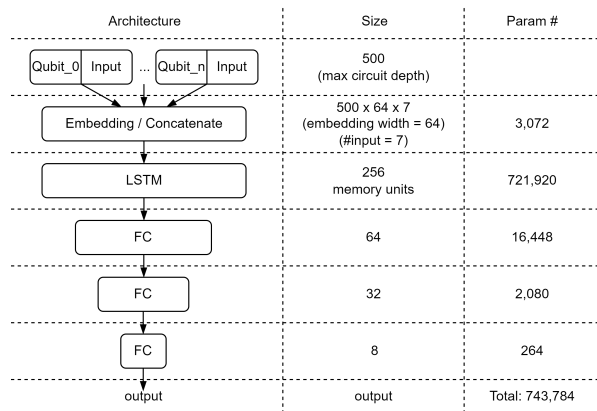


FIG. 10. Neural Network architecture of Q-fid. The number of input layers depends on the number of qubits inside a processor, this figure is showing the architecture for *ibm_nairobi*.

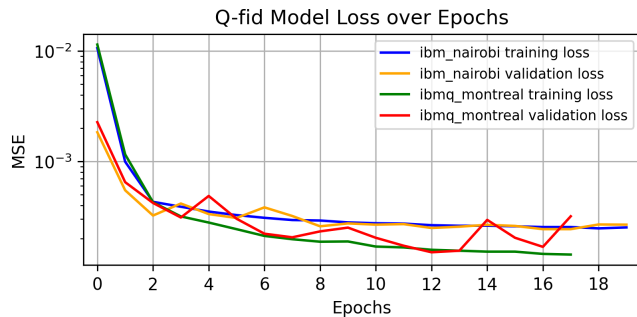


FIG. 11. Training loss and validation loss for the two datasets. Training terminated on epoch 20 for *ibm_nairobi*, and on epoch 18 for *ibmq_montreal*. The final validation loss is $0.150\text{E-}3$ for *ibm_nairobi*, and $0.243\text{E-}3$ for *ibmq_montreal*

label into a 64-dimensional dense vector and they are all concatenated together to represent one input timestep. The LSTM layer uses 256 memory units, followed by three fully-connected layers. We use ReLU activation and Sigmoid activation for the final layer. The model for *ibm_nairobi* contains 743,784 trainable parameters with 7 input layers, and the model for *ibmq_montreal* contains 7,403,004 trainable parameters with 27 input layers. The model for *ibmq_montreal* has mostly the same architecture, only changing the number of input layers and adding the number of hidden units.

The models are trained with a batch size of 32 plus Adam optimizer for 20 epochs using the MSE loss function, the training automatically terminates if the loss does not improve for 5 continuous epochs. The training, validation, and test split ratio is 7:2:1, we evaluate loss on the validation set and picked the best-performing model on the test set. The training curve for the two models is shown in figure 11, and figure 12 shows the scatter plot of real fidelity vs. predicted fidelity of Q-fid running on the test set.

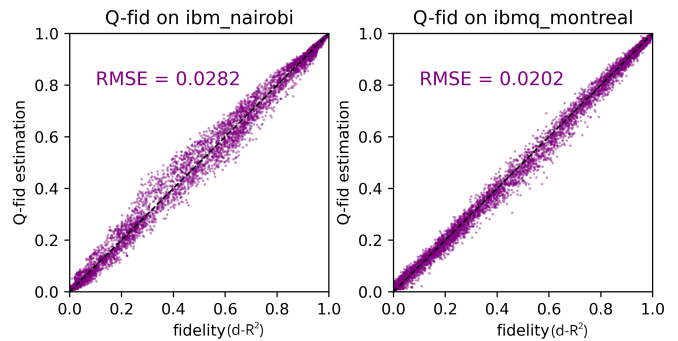


FIG. 12. Scatter plot of real fidelity vs. predicted fidelity of Q-fid running on the test set. The test set for *ibm_nairobi* contains 8,265 data points, and the test set for *ibmq_montreal* contains 9,140 data points

V. RESULTS AND DISCUSSION

A. Fidelity Prediction

Based on the number of qubits, connection complexity, and algorithm practicality, we picked 25 quantum circuits from the QASMBench [16] NISQ benchmark suite to demonstrate the performance of Q-fid. Figure 13 shows four representative samples from the full result: Hidden Subgroup problem (*hs4_n4*) [34], Quantum Ripple Carry Adder (*adder_n4*) [34], Variational Ansatz (*variational_n4*) [35], and Quantum Fourier Transform (*qft_n4*) [36].

Each circuit is simulated 50 times with 1,024 shots on the Qiskit Aer simulator [37] with a noise model that mimics *ibm_nairobi*. The RMSE of Q-fid’s prediction ranges from 0.003 to 0.182 with an average of 0.0515. On the other hand, *mapomatic*’s fidelity estimation has an average RMSE of 0.142, with a minimum RMSE equal to 0.0424 and a maximum RMSE of 0.284. On the Quantum Walks algorithm (*quantumwalks_n2*) [38], Q-fid’s prediction is $24.7\times$ more accurate than *mapomatic*.

All of the 25 circuits in this section are not optimized for physical qubit layout, so the logical qubits are placed on *ibm_nairobi* in numerical order from physical qubit 0 to physical qubit 6 and stay on the same layout for all 50 trials. Because most of the test circuits are placed on the same physical qubits, the variables in this experiment are the different quantum gates used in different algorithms. The results prove that Q-fid has learned the noise characteristics of different quantum gates on the same physical qubit from the training circuits. In contrast, the error rate based *mapomatic* tends to give an underestimation, especially for high-fidelity circuits.

The full experiment result and data are available in Appendix A: figure 16, and table II.

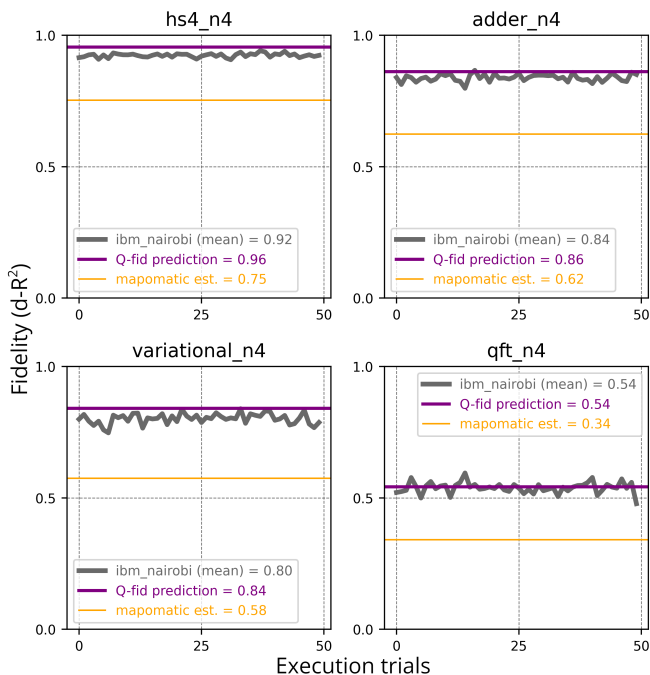


FIG. 13. Q-fid’s fidelity prediction (purple) compared with `mapomatic` (orange) on `ibmq_nairobi`. Due to the probabilistic nature of quantum state measurements, the fidelity for the same circuit varies every time when executed even with the same device noise model (gray). So each quantum circuit is executed with 1,024 shots to obtain its output distribution, then repeated 50 times (x-axis) to calculate its mean fidelity. Q-fid accurately predicts the mean fidelity of each circuit.

B. Transpilation Optimizations

Figure 14 shows the same four sample circuits mentioned in section V A running on `ibmq_montreal`. In this experiment, the transpiler optimization is on and the physical qubit layouts are no longer fixed. Since `ibmq_montreal` is a 27-qubit processor, a circuit only using 4 physical qubits can have many available layout options depending on the number of CNOT gates it contains. For example, the `hs4_n4` circuit has a depth of 34 and 13 CNOT gates, and it has a total of 2,728 different layouts shown on the x-axis, ranked from the highest fidelity layout to the lowest fidelity layout.

Q-fid accurately tracks the fidelity of different layouts for all 25 test circuits, with the number of CNOT gates in the circuits ranging from 1 to 1,419. Considering the predicted fidelities for all the layouts, Q-fid achieves an average RMSE of 0.0459, which is $5.95\times$ (up to $14.9\times$) better than `mapomatic`. When looking at only the top 10% of layouts, Q-fid achieves an average RMSE of 0.0252, which is $12.3\times$ (up to $32.8\times$) better than `mapomatic`.

An important difference should be addressed for this experiment compared with the previous experiment in section V A: In the previous experiment, the circuits are executed on fixed physical layouts, so the objective is to test if Q-fid can learn the effects of **different quan-**

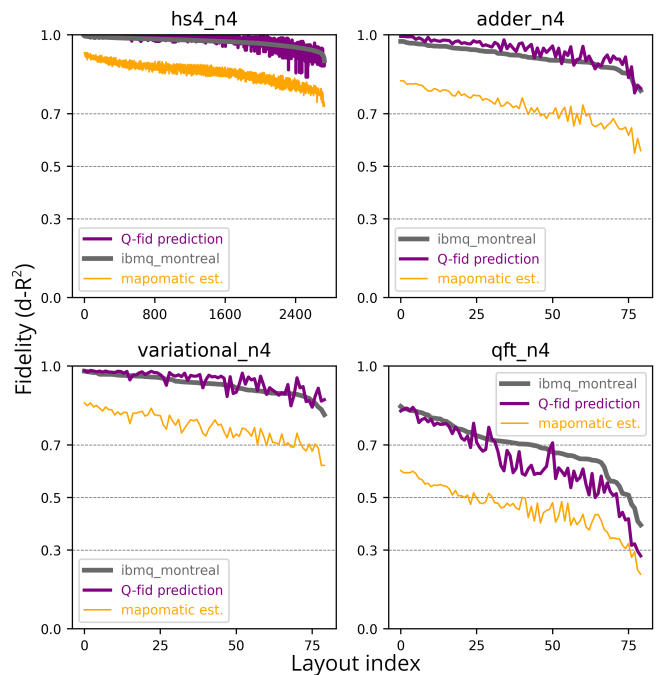


FIG. 14. Q-fid’s fidelity prediction (purple) for different circuit layouts on `ibmq_montreal`. The x-axis is the index of layouts for the quantum circuit, the y-axis shows different $d-R^2$ fidelity score regions listed in table I. The order of the data is sorted from the highest fidelity layout to the lowest fidelity layout according to the fidelity reported by `ibmq_montreal` (gray). Q-fid accurately tracks the fidelity variance of every layout for each circuit.

tum gates when they are applied to the **same physical qubits**. However, in this experiment, the same circuits are placed and executed with different layouts, so the new objective here is to test if Q-fid can learn the effects when the **same quantum gates** are placed on **different physical qubits**.

The full experiment result and data are available in Appendix A: figure 17, and table III.

C. Noise-adaptive Training

Since the noise characteristic of a quantum processor is constantly changing, it is important to make sure that Q-fid can adapt to this change over time. Figure 15 shows how Q-fid can still give an accurate fidelity prediction even after the device noise model has changed. In figure 15, the same experiment in section V A was performed again, but the noise model of `ibmq_nairobi` is changed to Nov. 18, 2022, three days later than the first experiment. The new noise model has a slightly worse fidelity performance than the previous one, which is shown to the right of the blue vertical line.

The RMSE of Q-fid’s new prediction ranges from 0.002 to 0.223 with an average of 0.0653. On the other hand, `mapomatic`’s new fidelity estimation has an aver-

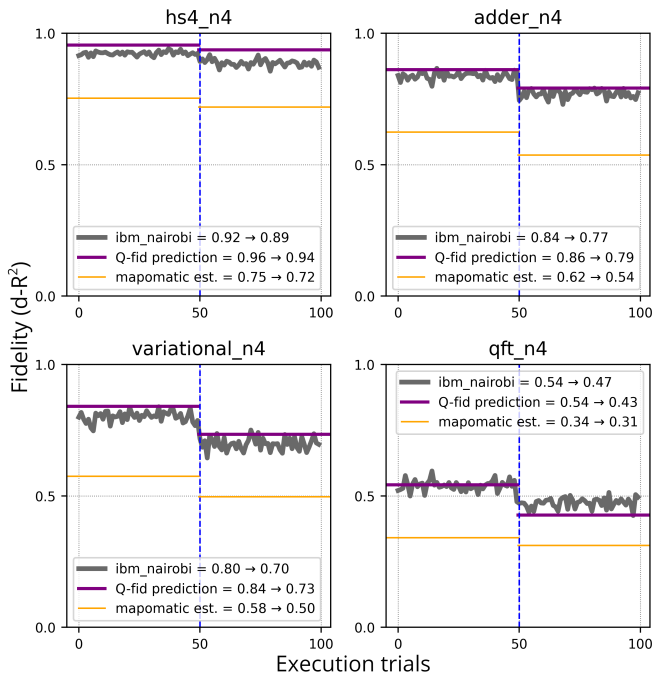


FIG. 15. Q-fid’s fidelity prediction (purple) compared with `mapomatic` (orange) on `ibm_nairobi`. Again, the fidelity for the same circuit varies every time when executed (gray) due to the probabilistic nature of quantum state measurement. The first 50 trials (left of the blue line) are performed on Nov. 15, 2022, which is the same data as in figure 13. The next 50 trails (right of the blue line) were performed on Nov. 18, 2022, which shows that `ibm_nairobi`’s performance is slightly worse due to different noise patterns. Q-fid adapts to this new noise pattern and it only takes 100 new RB samples to retrain.

age RMSE of 0.148, with a minimum RMSE equal to 0.0384 and a maximum RMSE of 0.287. For the new noise model, Q-fid’s prediction is $5.31\times$ more accurate than `mapomatic` on average, with the most accurate one being $42.0\times$ better.

More importantly, this experiment shows how efficiently Q-fid adapts to the new noise characteristics, since the new Q-fid predictions are made after only retraining the LSTM with 100 new QC samples. For Q-fid to update its internal parameters, it can use the output of any QC to retrain its LSTM, which means that Q-fid can be updated directly and continuously using the output from its own workload. In contrast, `mapomatic` needs to use the latest gate error rates to give updated predictions, which requires the processor to perform individual RB experiments for single-qubit gates, two-qubits gates, and measure the T_1/T_2 coherence times and error rates of the measurement gates. This process interrupts normal workflow and the prediction accuracy entirely depends on how recently the calibration jobs are performed.

The full experiment result and data are available in Appendix A: figure 18, and table II.

VI. RELATED WORK

Quantum gate fidelity and qubit noise are very active topics in NISQ research. Randomized benchmarking is one of the earliest protocols developed to characterize and quantify quantum operation error rates [14, 19, 39], and remains the most commonly used tool for this purpose today. The latest works focus on improving randomized benchmarking to support more quantum operations [40], and make the protocol more flexible for larger circuits consisting of many qubits [41, 42].

Given the high error rates of quantum gates, quantum circuits must be carefully implemented on real hardware to retrieve more useful measurements. Early research concentrated on circuit compilation techniques to improve the fidelity of the output. For example, using gate scheduling to reduce the number of physical quantum gates or rerouting the CNOT connections to minimize SWAP gates [43–46]. Recently, however, the research direction has shifted to hardware-specific optimization and noise-aware qubit mapping [11, 47–49]. Due to the constantly changing device calibration data, quantum circuits have to be transpiled according to the architecture and noise characteristics of the processor in order to achieve the best performance.

Fidelity estimation is an emerging research field in quantum computing. Although it has been proved that estimating the final fidelity from the quantum circuit description itself is hard in general, many works have demonstrated using quantum algorithms to attack this problem and achieving exponential speedup [50, 51]. Other approaches like statistical estimation and polynomial fitting were also investigated in [52] and [53]. Using machine learning for fidelity estimation is still a very new area of research. While most prior works train a shallow neural network to predict the fidelity of a quantum circuit [53–55], recent papers are expanding to explore different architectures. For example, using graph transformer as in [56].

VII. CONCLUSION

In this work, we present the Q-fid system to accurately predict the fidelity of a quantum circuit running on a real NISQ processor. We show that the performance of NISQ processors is easily affected by external noise, so with Q-fid’s fidelity prediction we can help save quantum computing resources by optimizing circuit layout and reducing execution shots, all before implementing the quantum circuit on real hardware. Q-fid uses LSTM to learn the noise properties of the qubit and the relationship between quantum gates, without the need for any separate input of hardware calibration data and gate error rates. A novel method to model the quantum circuits using text labels was presented, and the full training workflow was introduced. We proposed a new metric called $d-R^2$ to intuitively quantify the fidelity of a noisy quantum circuit,

and based on this metric, we also showed how to generate a training circuit dataset using Randomized Benchmarking circuits. We compared Q-fid’s performance with the `mapomatic` tool, and the results prove that Q-fid can effectively learn the characteristics of different qubits, gates, and the structure of quantum circuits.

ACKNOWLEDGMENTS

This work was supported by JST COI-NEXT Grant Number JPMJPF2221 and JST SPRING Grant Number

JPMJSP2123. We acknowledge the use of IBM Quantum services for this work. The views expressed are those of the authors, and do not reflect the official policy or position of IBM or the IBM Quantum team.

-
- [1] D. R. Simon, *SIAM Journal on Computing* **26**, 1474 (1997), <https://doi.org/10.1137/S0097539796298637>.
- [2] F. Arute, K. Arya, R. Babbush, D. Bacon, J. C. Bardin, R. Barends, R. Biswas, S. Boixo, F. G. S. L. Brandao, D. A. Buell, B. Burkett, Y. Chen, Z. Chen, B. Chiaro, R. Collins, W. Courtney, A. Dunsworth, E. Farhi, B. Foxen, A. Fowler, C. Gidney, M. Giustina, R. Graff, K. Guerin, S. Habegger, M. P. Harrigan, M. J. Hartmann, A. Ho, M. Hoffmann, T. Huang, T. S. Humble, S. V. Isakov, E. Jeffrey, Z. Jiang, D. Kafri, K. Kechedzhi, J. Kelly, P. V. Klimov, S. Knysh, A. Korotkov, F. Kostritsa, D. Landhuis, M. Lindmark, E. Lucero, D. Lyakh, S. Mandrà, J. R. McClean, M. McEwen, A. Megrant, X. Mi, K. Michielsen, M. Mohseni, J. Mutus, O. Naaman, M. Neeley, C. Neill, M. Y. Niu, E. Ostby, A. Petukhov, J. C. Platt, C. Quintana, E. G. Rieffel, P. Roushan, N. C. Rubin, D. Sank, K. J. Satzinger, V. Smelyanskiy, K. J. Sung, M. D. Trevithick, A. Vainsencher, B. Villalonga, T. White, Z. J. Yao, P. Yeh, A. Zalcman, H. Neven, and J. M. Martinis, *Nature* **574**, 505 (2019).
- [3] C. Wang, X. Li, H. Xu, Z. Li, J. Wang, Z. Yang, Z. Mi, X. Liang, T. Su, C. Yang, G. Wang, W. Wang, Y. Li, M. Chen, C. Li, K. Linghu, J. Han, Y. Zhang, Y. Feng, Y. Song, T. Ma, J. Zhang, R. Wang, P. Zhao, W. Liu, G. Xue, Y. Jin, and H. Yu, *Transmon qubit with relaxation time exceeding 0.5 milliseconds* (2021).
- [4] A. Ortu, A. Holzäpfel, J. Etesse, and M. Afzelius, *npj Quantum Information* **8**, 10.1038/s41534-022-00541-3 (2022).
- [5] J. Preskill, *Quantum* **2**, 79 (2018).
- [6] Z. Cai, R. Babbush, S. C. Benjamin, S. Endo, W. J. Huggins, Y. Li, J. R. McClean, and T. E. O’Brien, *Quantum error mitigation* (2022).
- [7] K. Temme, S. Bravyi, and J. M. Gambetta, *Phys. Rev. Lett.* **119**, 180509 (2017).
- [8] H.-L. Huang, X.-Y. Xu, C. Guo, G. Tian, S.-J. Wei, X. Sun, W.-S. Bao, and G.-L. Long, *Near-term quantum computing techniques: Variational quantum algorithms, error mitigation, circuit compilation, benchmarking and classical simulation* (2022).
- [9] Y. Ueno, M. Kondo, M. Tanaka, Y. Suzuki, and Y. Tabuchi, in *2021 58th ACM/IEEE Design Automation Conference (DAC)* (2021) pp. 451–456.
- [10] Y. Ueno, M. Kondo, M. Tanaka, Y. Suzuki, and Y. Tabuchi, in *2022 IEEE International Symposium on High-Performance Computer Architecture (HPCA)* (2022) pp. 274–287.
- [11] M. Y. Siraichi, V. F. dos Santos, C. Collange, and F. M. Q. Pereira, in *Proceedings of the 2018 International Symposium on Code Generation and Optimization* (ACM, 2018).
- [12] S. S. Tannu and M. K. Qureshi, in *Proceedings of the Twenty-Fourth International Conference on Architectural Support for Programming Languages and Operating Systems* (ACM, 2019).
- [13] P. D. Nation and M. Treinish, *Suppressing quantum circuit errors due to system variability* (2022).
- [14] E. Magesan, J. M. Gambetta, and J. Emerson, *Physical Review Letters* **106**, 10.1103/physrevlett.106.180504 (2011).
- [15] T. Proctor, K. Rudinger, K. Young, E. Nielsen, and R. Blume-Kohout, *Nature Physics* **18**, 75 (2021).
- [16] A. Li, S. Stein, S. Krishnamoorthy, and J. Ang, *Qasm-bench: A low-level qasm benchmark suite for nisq evaluation and simulation* (2020).
- [17] IBM, *IBM Quantum* (2021).
- [18] E. Bernstein and U. Vazirani, *SIAM Journal on Computing* **26**, 1411 (1997), <https://doi.org/10.1137/S0097539796300921>.
- [19] E. Magesan, J. M. Gambetta, and J. Emerson, *Physical Review A* **85**, 10.1103/physreva.85.042311 (2012).
- [20] S. Bravyi and D. Maslov, *IEEE Transactions on Information Theory* **67**, 4546 (2021).
- [21] S. Hochreiter and J. Schmidhuber, *Neural Comput.* **9**, 1735–1780 (1997).
- [22] H. Palangi, L. Deng, Y. Shen, J. Gao, X. He, J. Chen, X. Song, and R. Ward, *IEEE/ACM Transactions on Audio, Speech, and Language Processing* **24**, 694 (2016).
- [23] D. Chicco, M. J. Warrens, and G. Jurman, *PeerJ Computer Science* **7**, e623 (2021).
- [24] J. Liu and H. Zhou, in *2020 IEEE International Symposium on Workload Characterization (IISWC)* (2020) pp. 94–105.
- [25] D. Oliveira, E. Giusto, B. Baheri, Q. Guan, B. Montrucchio, and P. Rech, *A systematic methodology to compute the quantum vulnerability factors for quantum circuits* (2021).
- [26] T. Patel, D. Silver, and D. Tiwari, *Charter: Identifying the most-critical gate operations in quantum circuits via amplified gate reversibility* (2022).

- [27] E. Farhi, J. Goldstone, and S. Gutmann, [A quantum approximate optimization algorithm](#) (2014).
- [28] A. Peruzzo, J. McClean, P. Shadbolt, M.-H. Yung, X.-Q. Zhou, P. J. Love, A. Aspuru-Guzik, and J. L. O’Brien, *Nature Communications* **5**, [10.1038/ncomms5213](#) (2014).
- [29] A. Deshpande, P. Niroula, O. Shtanko, A. V. Gorshkov, B. Fefferman, and M. J. Gullans, *PRX Quantum* **3**, [040329](#) (2022).
- [30] K. Tamura and Y. Shikano, in *International Symposium on Mathematics, Quantum Theory, and Cryptography* (Springer Singapore, 2020) pp. 17–37.
- [31] M. Dwarampudi and N. V. S. Reddy, [Effects of padding on lstms and cnns](#) (2019).
- [32] T. Mikolov, K. Chen, G. Corrado, and J. Dean, Efficient estimation of word representations in vector space (2013), [arXiv:1301.3781 \[cs.CL\]](#).
- [33] D. Gottesman, in *Group theoretical methods in physics* (1998).
- [34] A. JavadiAbhari, S. Patil, D. Kudrow, J. Heckey, A. Lvov, F. T. Chong, and M. Martonosi, in *Proceedings of the 11th ACM Conference on Computing Frontiers* (ACM, 2014).
- [35] J. R. McClean, N. C. Rubin, K. J. Sung, I. D. Kivlichan, X. Bonet-Monroig, Y. Cao, C. Dai, E. S. Fried, C. Gidney, B. Gimby, P. Gokhale, T. Häner, T. Hardikar, V. Havlíček, O. Higgott, C. Huang, J. Izaac, Z. Jiang, X. Liu, S. McArdle, M. Neeley, T. O’Brien, B. O’Gorman, I. Ozfidan, M. D. Radin, J. Romero, N. P. D. Sawaya, B. Senjean, K. Setia, S. Sim, D. S. Steiger, M. Steudtner, Q. Sun, W. Sun, D. Wang, F. Zhang, and R. Babbush, *Quantum Science and Technology* **5**, [034014](#) (2020).
- [36] A. Cross, A. Javadi-Abhari, T. Alexander, N. D. Beaudrap, L. S. Bishop, S. Heidel, C. A. Ryan, P. Sivarajah, J. Smolin, J. M. Gambetta, and B. R. Johnson, *ACM Transactions on Quantum Computing* **3**, [1](#) (2022).
- [37] M. Treinish, J. Gambetta, Soolu Thomas, P. Nation, Qiskit-Bot, P. Kassebaum, D. M. Rodríguez, S. De La Puente González, J. Lishman, Shaohan Hu, L. Bello, J. Garrison, K. Krsulich, Junye Huang, J. Yu, M. Marques, J. Gacon, D. McKay, E. Arellano, J. Gomez, L. Capelluto, Travis-S-IBM, A. Mitchell, A. Panigrahi, Lerongil, Rafey Iqbal Rahman, S. Wood, Toshinari Itoko, A. Pozas-Kerstjens, and C. J. Wood, *Qiskit/qiskit: Qiskit 0.42.0* (2023).
- [38] <https://github.com/raffmiceli>, Qiskit code to simulate quantum walks on graphs with up to 4 nodes, https://github.com/raffmiceli/Quantum_Walks (2020), [Accessed 16-Mar-2023].
- [39] E. Knill, D. Leibfried, R. Reichle, J. Britton, R. B. Blakestad, J. D. Jost, C. Langer, R. Ozeri, S. Seidelin, and D. J. Wineland, *Physical Review A* **77**, [10.1103/physreva.77.012307](#) (2008).
- [40] D. C. McKay, S. Sheldon, J. A. Smolin, J. M. Chow, and J. M. Gambetta, *Physical Review Letters* **122**, [10.1103/physrevlett.122.200502](#) (2019).
- [41] T. Proctor, S. Seritan, K. Rudinger, E. Nielsen, R. Blume-Kohout, and K. Young, *Physical Review Letters* **129**, [10.1103/physrevlett.129.150502](#) (2022).
- [42] J. Helsen, X. Xue, L. M. K. Vandersypen, and S. Wehner, A new class of efficient randomized benchmarking protocols (2019), [arXiv:1806.02048 \[quant-ph\]](#).
- [43] K. E. C. Booth, M. Do, J. C. Beck, E. Rieffel, D. Venturelli, and J. Frank, Comparing and integrating constraint programming and temporal planning for quantum circuit compilation (2018), [arXiv:1803.06775 \[quant-ph\]](#).
- [44] G. G. Guerreschi and J. Park, *Quantum Science and Technology* **3**, [045003](#) (2018).
- [45] A. Paler, A. Zulehner, and R. Wille, Nisq circuit compilation is the travelling salesman problem on a torus (2021), [arXiv:1806.07241 \[quant-ph\]](#).
- [46] G. Li, Y. Ding, and Y. Xie, Tackling the qubit mapping problem for nisq-era quantum devices (2019), [arXiv:1809.02573 \[cs.ET\]](#).
- [47] S. S. Tannu and M. K. Qureshi, A case for variability-aware policies for nisq-era quantum computers (2018), [arXiv:1805.10224 \[quant-ph\]](#).
- [48] S. Nishio, Y. Pan, T. Satoh, H. Amano, and R. V. Meter, *ACM Journal on Emerging Technologies in Computing Systems* **16**, [1](#) (2020).
- [49] S. S. Tannu and M. Qureshi, in *Proceedings of the 52nd Annual IEEE/ACM International Symposium on Microarchitecture*, MICRO ’52 (Association for Computing Machinery, New York, NY, USA, 2019) p. 253–265.
- [50] A. Gilyén and A. Poremba, Improved quantum algorithms for fidelity estimation (2022), [arXiv:2203.15993 \[quant-ph\]](#).
- [51] Q. Wang, Z. Zhang, K. Chen, J. Guan, W. Fang, J. Liu, and M. Ying, *IEEE Transactions on Information Theory* **69**, [273](#) (2023).
- [52] X.-D. Yu, J. Shang, and O. Gühne, *Advanced Quantum Technologies* **5**, [2100126](#) (2022).
- [53] J. Liu and H. Zhou, in *2020 IEEE International Symposium on Workload Characterization (IISWC)* (2020) pp. 94–105.
- [54] X. Zhang, M. Luo, Z. Wen, Q. Feng, S. Pang, W. Luo, and X. Zhou, *Phys. Rev. Lett.* **127**, [130503](#) (2021).
- [55] A. Vadali, R. Kshirsagar, P. Shyamsundar, and G. N. Perdue, Quantum circuit fidelity estimation using machine learning (2023), [arXiv:2212.00677 \[quant-ph\]](#).
- [56] H. Wang, P. Liu, J. Cheng, Z. Liang, J. Gu, Z. Li, Y. Ding, W. Jiang, Y. Shi, X. Qian, D. Z. Pan, F. T. Chong, and S. Han, Quest: Graph transformer for quantum circuit reliability estimation (2022), [arXiv:2210.16724 \[quant-ph\]](#).

Appendix A: Experiment Results

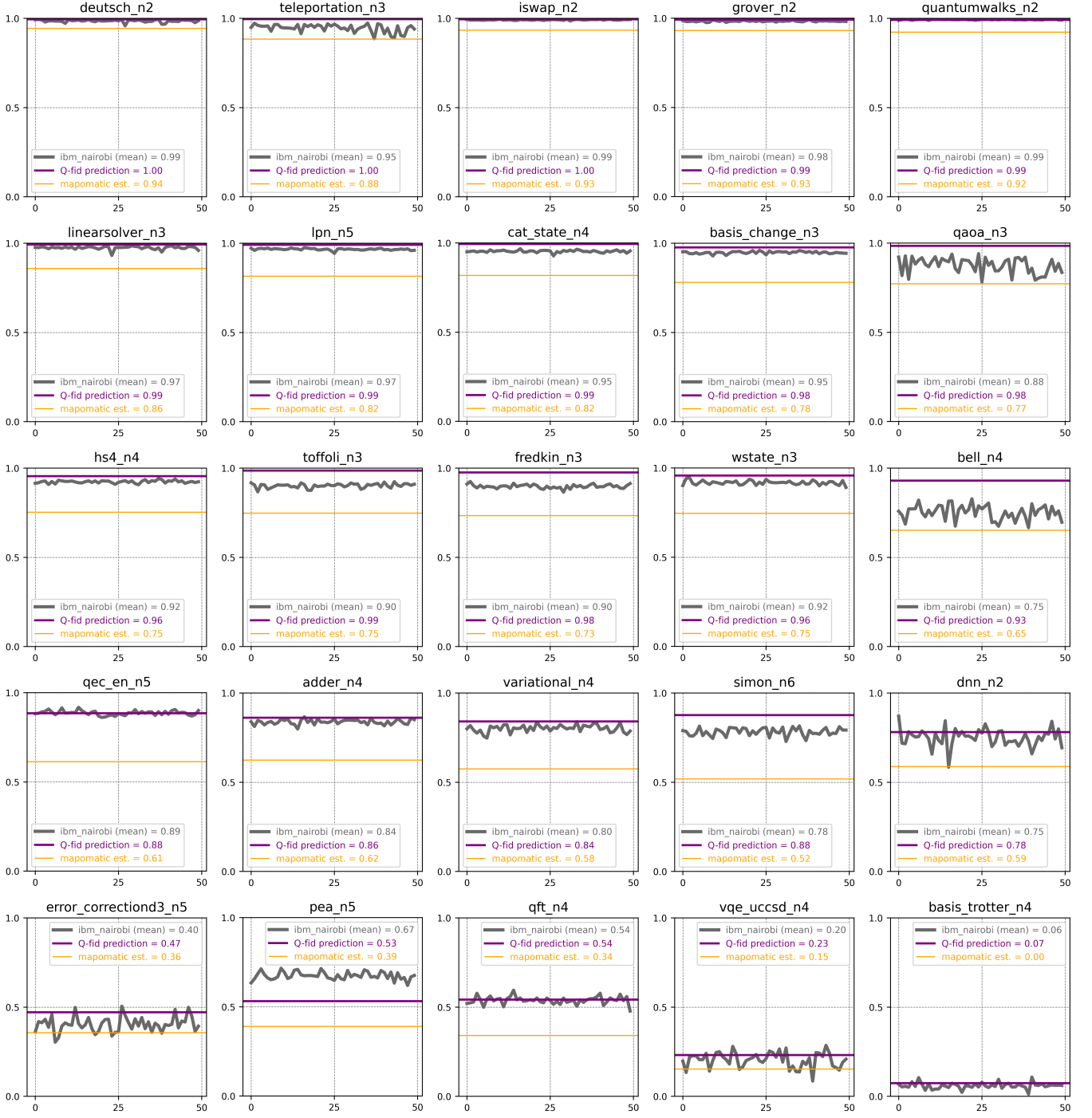


FIG. 16. Q-fid's fidelity prediction (purple) on *ibm_nairobi* compared with *mapomatic* (orange). The circuits are ranked from the lowest CNOT count (*deutsch_2*, top-left) to the highest CNOT count (*basis_trotter_n4*, bottom-right). Full data is available in table II.

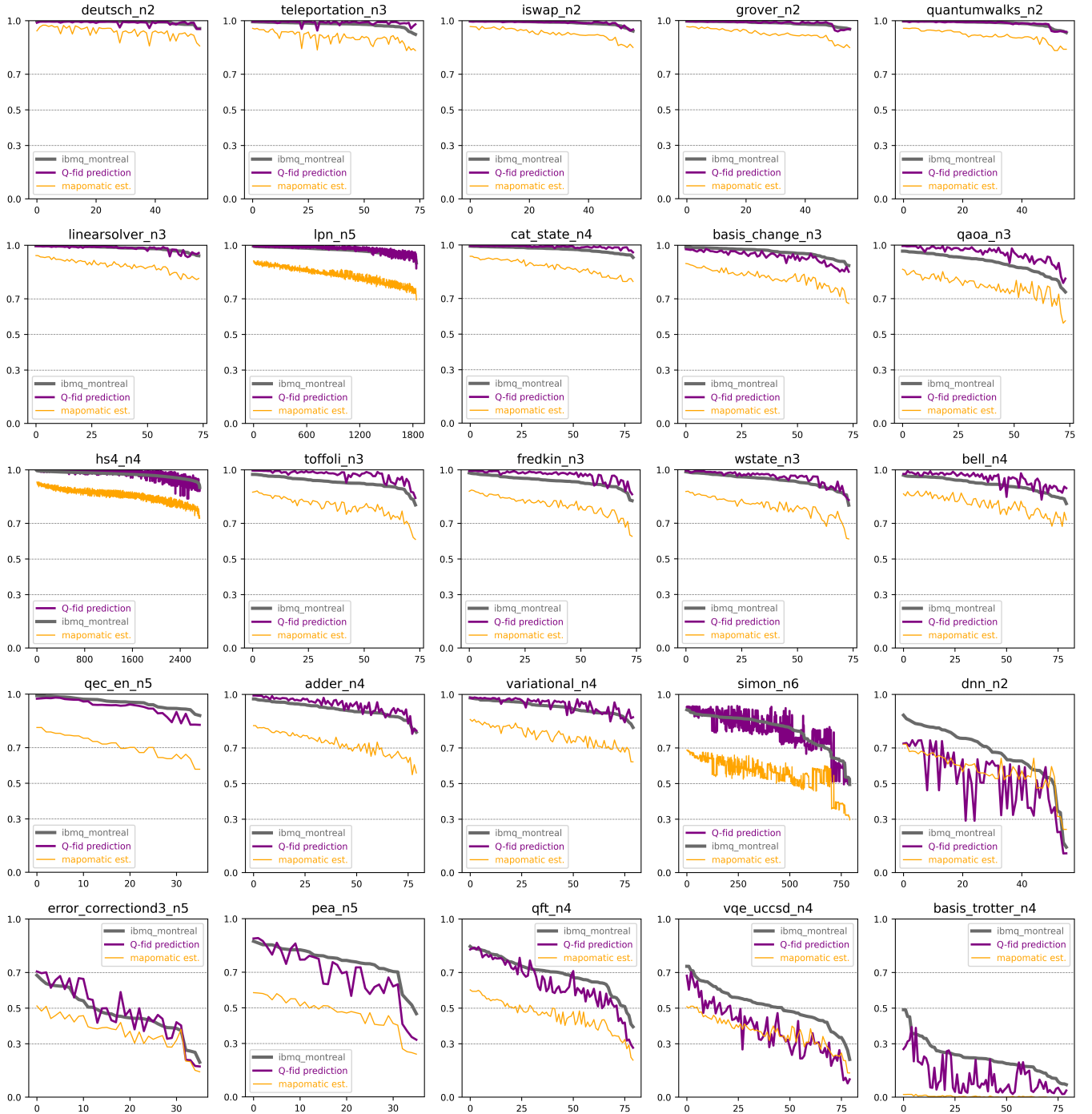


FIG. 17. Q-fid's fidelity prediction for different circuit layouts on *ibmq_montreal*. The x-axis is the index of layouts for the quantum circuit, the y-axis shows different $d-R^2$ score regions listed in table I. The circuits are ranked from the lowest CNOT count (*deutsch_2*, top-left) to the highest CNOT count (*basis_trotter_n4*, bottom-right). Full data is available in table III.

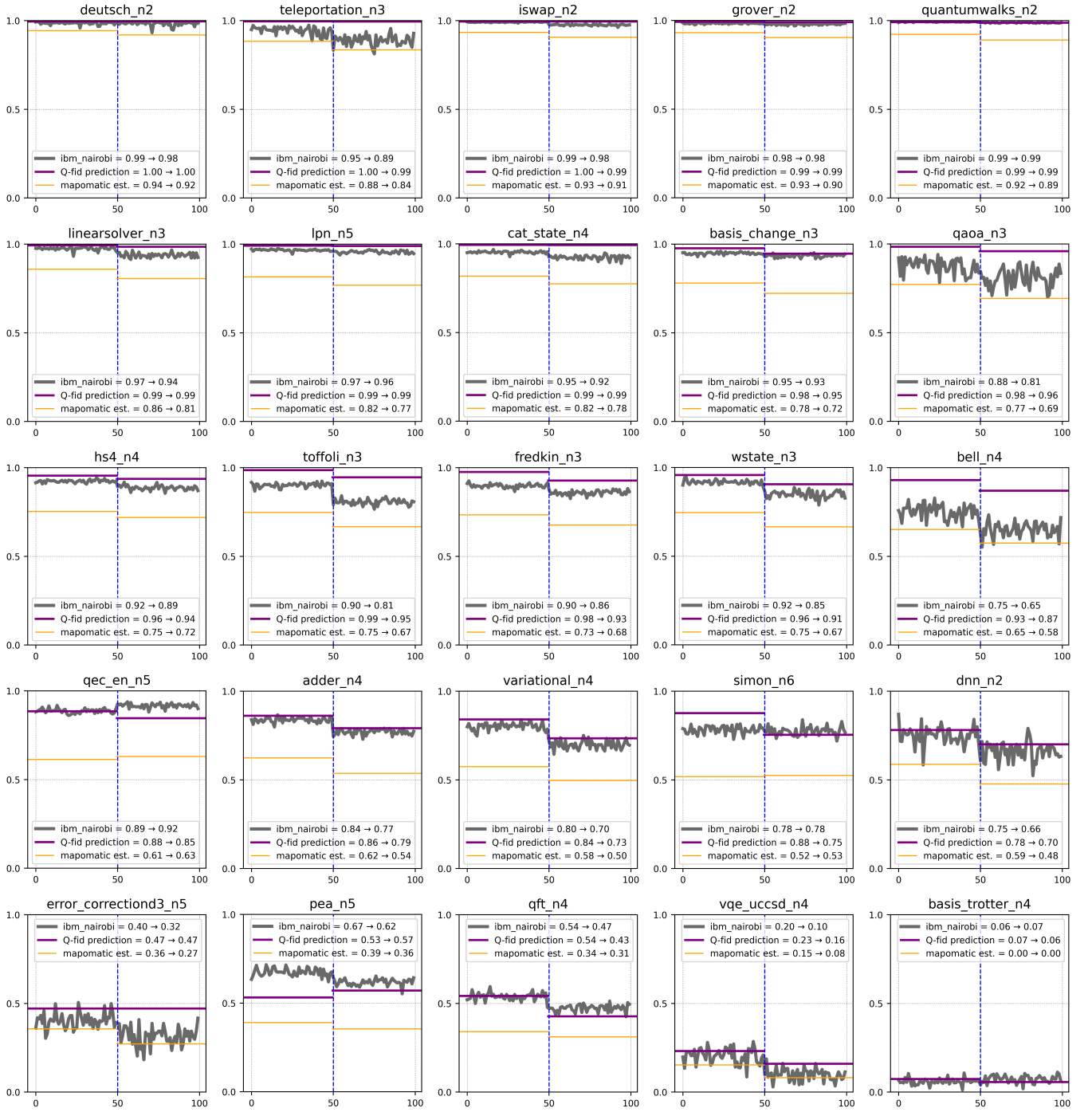


FIG. 18. Q-fid's fidelity prediction (purple) compared with mapomatic (orange) on *ibm_nairobi*. The first 50 trials (left to the blue line) are performed on Nov. 15, 2022, which is the same data as in figure 16. The next 50 trials (right to the blue line) are performed on Nov. 18, 2022, which shows that *ibm_nairobi*'s performance is slightly worse due to different noise patterns. Full data is available in table II.

| | Depth | #CNOT | <i>ibm_nairobi</i> mean fidelity (11/15, 2022) | <i>mapomatic</i> prediction (11/15) | <i>mapomatic</i> RMSE (11/15) | Q-fid prediction (11/15) | Q-fid RMSE (11/15) | <i>ibm_nairobi</i> mean fidelity (11/18, 2022) | <i>mapomatic</i> prediction (11/18) | <i>mapomatic</i> RMSE (11/18) | Q-fid prediction (11/18) | Q-fid RMSE (11/18) |
|-----------------------|-------|-------|--|---|-------------------------------------|--------------------------------|--------------------------|--|---|-------------------------------------|--------------------------------|--------------------------|
| deutsch_n2 | 9 | 1 | 0.99 | 0.9439 | 4.24E-02 | 0.9951 | 1.17E-02 | 0.98 | 0.9195 | 6.42E-02 | 0.9961 | 1.79E-02 |
| teleportation_n3 | 13 | 2 | 0.95 | 0.8844 | 6.52E-02 | 0.9957 | 5.46E-02 | 0.89 | 0.8359 | 6.01E-02 | 0.9950 | 1.10E-01 |
| iswap_n2 | 14 | 2 | 0.99 | 0.9347 | 5.73E-02 | 0.9953 | 3.79E-03 | 0.98 | 0.9067 | 6.93E-02 | 0.9950 | 1.94E-02 |
| grover_n2 | 26 | 2 | 0.98 | 0.9321 | 5.16E-02 | 0.9923 | 9.28E-03 | 0.98 | 0.9040 | 7.48E-02 | 0.9905 | 1.26E-02 |
| quantumwalks_n2 | 24 | 3 | 0.99 | 0.9229 | 7.07E-02 | 0.9913 | 2.86E-03 | 0.99 | 0.8912 | 9.76E-02 | 0.9884 | 2.33E-03 |
| linearsolver_n3 | 29 | 4 | 0.97 | 0.8591 | 1.16E-01 | 0.9934 | 2.05E-02 | 0.94 | 0.8063 | 1.32E-01 | 0.9854 | 4.90E-02 |
| lpn_n5 | 12 | 5 | 0.97 | 0.8156 | 1.51E-01 | 0.9919 | 2.59E-02 | 0.96 | 0.7696 | 1.86E-01 | 0.9897 | 3.47E-02 |
| cat_state_n4 | 10 | 6 | 0.95 | 0.8182 | 1.35E-01 | 0.9944 | 4.16E-02 | 0.92 | 0.7750 | 1.49E-01 | 0.9933 | 7.06E-02 |
| basis_change_n3 | 114 | 10 | 0.95 | 0.7811 | 1.67E-01 | 0.9769 | 2.94E-02 | 0.93 | 0.7231 | 2.12E-01 | 0.9463 | 1.42E-02 |
| qaoa_n3 | 24 | 12 | 0.88 | 0.7729 | 1.12E-01 | 0.9846 | 1.17E-01 | 0.81 | 0.6942 | 1.26E-01 | 0.9599 | 1.59E-01 |
| hs4_n4 | 34 | 13 | 0.92 | 0.7539 | 1.70E-01 | 0.9552 | 3.20E-02 | 0.89 | 0.7201 | 1.67E-01 | 0.9368 | 5.12E-02 |
| toffoli_n3 | 23 | 15 | 0.90 | 0.7483 | 1.54E-01 | 0.9863 | 8.49E-02 | 0.81 | 0.6681 | 1.39E-01 | 0.9460 | 1.41E-01 |
| fredkin_n3 | 25 | 17 | 0.90 | 0.7344 | 1.64E-01 | 0.9764 | 7.89E-02 | 0.86 | 0.6773 | 1.83E-01 | 0.9280 | 6.98E-02 |
| wstate_n3 | 37 | 18 | 0.92 | 0.7464 | 1.72E-01 | 0.9575 | 4.12E-02 | 0.85 | 0.6659 | 1.84E-01 | 0.9060 | 6.06E-02 |
| bell_n4 | 62 | 25 | 0.75 | 0.6524 | 1.08E-01 | 0.9301 | 1.82E-01 | 0.65 | 0.5750 | 8.55E-02 | 0.8707 | 2.23E-01 |
| qec_en_n5 | 45 | 31 | 0.89 | 0.6143 | 2.73E-01 | 0.8848 | 1.26E-02 | 0.92 | 0.6307 | 2.87E-01 | 0.8459 | 7.22E-02 |
| adder_n4 | 48 | 40 | 0.84 | 0.6246 | 2.14E-01 | 0.8616 | 2.67E-02 | 0.77 | 0.5373 | 2.34E-01 | 0.7916 | 2.62E-02 |
| variational_n4 | 70 | 40 | 0.80 | 0.5756 | 2.27E-01 | 0.841 | 4.38E-02 | 0.70 | 0.4970 | 2.03E-01 | 0.7343 | 4.28E-02 |
| simon_n6 | 57 | 41 | 0.78 | 0.5188 | 2.65E-01 | 0.8762 | 9.60E-02 | 0.78 | 0.5263 | 2.50E-01 | 0.7543 | 3.15E-02 |
| dnn_n2 | 499 | 42 | 0.75 | 0.5883 | 1.70E-01 | 0.7814 | 5.77E-02 | 0.66 | 0.4773 | 1.90E-01 | 0.7011 | 6.53E-02 |
| error_correctiond3_n5 | 163 | 79 | 0.40 | 0.3572 | 6.36E-02 | 0.4715 | 7.94E-02 | 0.32 | 0.2726 | 6.92E-02 | 0.4710 | 1.63E-01 |
| pea_n5 | 121 | 84 | 0.67 | 0.3910 | 2.84E-01 | 0.5322 | 1.44E-01 | 0.62 | 0.3556 | 2.63E-01 | 0.5713 | 5.01E-02 |
| qft_n4 | 132 | 87 | 0.54 | 0.3414 | 1.99E-01 | 0.5424 | 2.10E-02 | 0.47 | 0.3119 | 1.63E-01 | 0.4273 | 5.00E-02 |
| vqe_uccsd_n4 | 351 | 166 | 0.20 | 0.1532 | 6.66E-02 | 0.2312 | 4.98E-02 | 0.10 | 0.0814 | 3.84E-02 | 0.1593 | 6.90E-02 |
| basis_trotter_n4 | 2593 | 1419 | 0.06 | 0.0000 | 6.22E-02 | 0.0739 | 2.19E-02 | 0.07 | 0.0000 | 7.59E-02 | 0.0566 | 2.62E-02 |

TABLE II. Fidelity prediction data corresponding to figure 16 and figure 18.

| | <i>ibmq_montreal</i> fidelity range | #Layouts (all) | <i>mapomatic</i> RMSE (all) | Q-fid RMSE (all) | #Layouts (top 10%) | <i>mapomatic</i> RMSE (top 10%) | Q-fid RMSE (top 10%) |
|-----------------------|--|-------------------|--------------------------------|---------------------|-----------------------|------------------------------------|-------------------------|
| deutsch_n2 | 1.00-0.96 | 56 | 5.965E-02 | 8.395E-03 | 6 | 3.409E-02 | 5.438E-03 |
| teleportation_n3 | 0.99-0.92 | 74 | 7.552E-02 | 1.660E-02 | 7 | 4.285E-02 | 2.216E-03 |
| iswap_n2 | 1.00-0.94 | 56 | 6.327E-02 | 4.743E-03 | 6 | 3.715E-02 | 3.496E-03 |
| grover_n2 | 1.00-0.95 | 56 | 6.307E-02 | 7.142E-03 | 6 | 3.381E-02 | 1.458E-03 |
| quantumwalks_n2 | 1.00-0.93 | 56 | 7.280E-02 | 4.874E-03 | 6 | 4.109E-02 | 3.736E-03 |
| linearsolver_n3 | 1.00-0.94 | 74 | 1.009E-01 | 8.393E-03 | 7 | 6.113E-02 | 3.097E-03 |
| lpn_n5 | 1.00-0.90 | 1840 | 1.400E-01 | 1.131E-02 | 184 | 9.545E-02 | 2.911E-03 |
| cat_state_n4 | 0.99-0.93 | 80 | 1.034E-01 | 1.724E-02 | 8 | 6.539E-02 | 2.597E-03 |
| basis_change_n3 | 0.99-0.89 | 74 | 1.438E-01 | 2.727E-02 | 7 | 1.023E-01 | 1.511E-02 |
| qaoa_n3 | 0.97-0.74 | 74 | 1.322E-01 | 5.724E-02 | 7 | 1.148E-01 | 3.079E-02 |
| hs4_n4 | 1.00-0.90 | 2728 | 1.191E-01 | 1.388E-02 | 273 | 8.007E-02 | 2.522E-03 |
| toffoli_n3 | 0.97-0.80 | 74 | 1.367E-01 | 4.377E-02 | 7 | 1.013E-01 | 2.356E-02 |
| fredkin_n3 | 0.98-0.83 | 74 | 1.356E-01 | 3.650E-02 | 7 | 1.012E-01 | 1.633E-02 |
| wstate_n3 | 0.99-0.80 | 74 | 1.486E-01 | 2.166E-02 | 7 | 1.154E-01 | 7.731E-03 |
| bell_n4 | 0.97-0.81 | 80 | 1.154E-01 | 3.922E-02 | 8 | 1.002E-01 | 1.889E-02 |
| qec_en_n5 | 0.99-0.88 | 36 | 2.453E-01 | 3.329E-02 | 4 | 1.896E-01 | 1.345E-02 |
| adder_n4 | 0.98-0.79 | 80 | 1.934E-01 | 2.981E-02 | 8 | 1.542E-01 | 2.102E-02 |
| variational_n4 | 0.98-0.82 | 80 | 1.633E-01 | 2.617E-02 | 8 | 1.273E-01 | 7.697E-03 |
| simon_n6 | 0.91-0.49 | 792 | 2.530E-01 | 5.100E-02 | 79 | 2.363E-01 | 2.280E-02 |
| dnn_n2 | 0.88-0.14 | 56 | 1.285E-01 | 1.873E-01 | 6 | 1.622E-01 | 1.292E-01 |
| error_correctiond3_n5 | 0.68-0.20 | 36 | 1.129E-01 | 5.624E-02 | 4 | 1.675E-01 | 3.887E-02 |
| pea_n5 | 0.87-0.47 | 36 | 2.900E-01 | 9.605E-02 | 4 | 2.817E-01 | 2.029E-02 |
| qft_n4 | 0.85-0.40 | 80 | 2.361E-01 | 7.141E-02 | 8 | 2.429E-01 | 1.835E-02 |
| vqe_uccsd_n4 | 0.73-0.21 | 80 | 1.536E-01 | 1.467E-01 | 8 | 1.965E-01 | 7.047E-02 |
| basis_trotter_n4 | 0.49-0.07 | 80 | 2.345E-01 | 1.319E-01 | 8 | 4.042E-01 | 1.486E-01 |

TABLE III. Transpilation optimization data corresponding to figure 17.